



1 **Decreasing trends of ammonia emissions over Europe seen**
2 **from remote sensing and inverse modelling**

3

4 **Ondřej Tichý¹, Sabine Eckhardt², Yves Balkanski³, Didier Hauglustaine³,**
5 **Nikolaos Evangeliou^{2,*}**

6

7 ¹The Czech Academy of Sciences, Institute of Information Theory and Automation, Prague,
8 Czech Republic.

9 ²Norwegian Institute for Air Research (NILU), Department of Atmospheric and Climate
10 Research (ATMOS), Kjeller, Norway.

11 ³Laboratoire des Sciences du Climat et de l'Environnement (LSCE), CEA-CNRS-UVSQ,
12 91191, Gif-sur-Yvette, France.

13

14 * Corresponding author: N. Evangeliou (Nikolaos.Evangeliou@nilu.no)

15



16 **Abstract**

17 Ammonia (NH₃), a significant precursor of particulate matter, is the most important
18 alkaline gas in the atmosphere and directly affects biodiversity, ecosystems, soil acidification.
19 It also indirectly affects climate and human health. In addition, its concentrations are constantly
20 rising because of the increasing feeding needs of the global population accompanied by a larger
21 use of fertilizers and animal farming. The combination of its increasing atmospheric levels with
22 its environmental and human impact has led many countries to adopt abatement strategies in
23 order to conform with respective regulations. While the significance of ammonia is pronounced,
24 its emissions are often associated with large uncertainties, while its atmospheric abundance is
25 difficult to measure. However, during the last decade, several satellite products have been
26 developed that measure ammonia very effectively, with low uncertainty, and most importantly,
27 with a global coverage. Here, we use satellite observations of column ammonia in combination
28 with an inversion algorithm to derive ammonia emissions with a high resolution over Europe
29 for the period 2013–2020.

30 Ammonia emissions peak in Northern Europe due to agricultural application and
31 livestock management and the local maxima are found over Western Europe (industrial
32 activity) and over Spain (pig farming). Our calculations show that these emissions have
33 decreased by -26% since 2013 (from 5431 Gg in 2013 to 3994 Gg in 2020) showing that the
34 abatement strategies adopted by the European Union have been very efficient. The slight
35 increase (+4.4%) reported in 2015 is also reproduced here and is attributed to some European
36 countries exceeding annual emission targets. Ammonia emissions are low in winter (286 Gg)
37 and peak in summer (563 Gg) and are dominated by the temperature dependent volatilization
38 of ammonia from the soil. The largest emission decreases were observed in Central and Eastern
39 Europe (-38%) and in Western Europe (-37%), while smaller decreases were recorded in
40 Northern (-17%) and Southern Europe (-7.6%). Our results are associated with relatively low
41 uncertainties reaching a maximum of 42%; when complemented against independent ground-
42 based observations, modelled concentrations using the posterior emissions showed improved
43 statistics, also following the observed seasonal trends. The posterior emissions presented here
44 also agree well with respective estimates reported in the literature and inferred from different
45 methodologies. These results indicate that the posterior emissions of ammonia calculated with
46 satellite measurements and combined with our adapted inverse modelling framework constitute
47 a robust basis for European NH₃ estimates and show the *de facto* evolution of ammonia
48 emissions since 2013.

49



50 **1 Introduction**

51 Ammonia (NH₃), the only alkaline gas in the atmosphere, constitutes one of the most
52 reactive nitrogen species. It is produced from decomposition of urea, which is a rapid process
53 when catalyzed by enzymes (Sigurdarson et al., 2018). The main sectors contributing to its
54 production are livestock management and wild animals (Behera et al., 2013), biomass burning
55 and domestic coal combustion (Fowler et al., 2004; Sutton et al., 2008), volcanic eruptions
56 (Sutton et al., 2008), and agriculture (Erisman et al., 2007). Emissions from agricultural activity
57 and livestock management represent over 80% of the total emissions (Crippa et al., 2020), while
58 their regional contribution can reach 94% (Van Damme et al., 2018).

59 Once emitted, it is transported over short distances and deposited to water bodies, soil or
60 vegetation with a typical atmospheric lifetime of a few hours (Evangelidou et al., 2021). It can
61 then lead to eutrophication of water bodies (Stevens et al., 2010), modulate soil pH (Galloway
62 et al., 2003) and «burn» vegetation by pulling water from the leaves (Krupa, 2003). It also reacts
63 with the abundant atmospheric sulfuric and nitric acids (Malm, 2004) forming fine particulate
64 matter (PM_{2.5}) (Tsimpidi et al., 2007). While ammonia has a short atmospheric lifetime, PM_{2.5}
65 resides significantly longer in the atmosphere, on the order of days to weeks (Seinfeld and
66 Pandis, 2000), and hence is transported over longer distances. Accordingly, secondary PM_{2.5}
67 can affect the Earth's radiative balance, both directly by scattering incoming radiation (Henze
68 et al., 2012) and indirectly as cloud condensation nuclei (Abbatt et al., 2006). Its environmental
69 effects include visibility problems and contribution to haze formation. Finally, PM_{2.5} affects
70 human health, as it penetrates the human respiratory system and deposits in the lungs and
71 alveolar regions (Pope and Dockery, 2006; Pope III et al., 2002) contributing to premature
72 mortality (Lelieveld et al., 2015).

73 To combat secondary pollution, the European Union established a set of measures
74 focusing on ammonia abatement, similar to the ones introduced by China (Giannakis et al.,
75 2019). These measures aim at reducing ammonia emissions by 6% in 2020, relative to 2005.
76 However, the lack of spatiotemporal measurements of ammonia over Europe makes any
77 assessment of the efficiency of these measures difficult, as only bottom-up methods are used to
78 calculate emission. These methods still show a slight increase (0.6% y⁻¹) up to 2018 mostly due
79 to increasing agricultural activities (McDuffie et al., 2020). Such bottom-up approaches rely on
80 uncertain land-use data and emission factors that are not always up to date, thus adding large
81 errors to existing inventories.



82 During the last decade, satellite products have also become available to fill the gaps
83 created by spatially disconnected ground-based measurements. Data from satellite sounders
84 such as the Infrared Atmospheric Sounding Interferometer (IASI) (Van Damme et al., 2017),
85 the Atmospheric Infrared Sounder (AIRS) (Warner et al., 2017), the Cross-track Infrared
86 Sounder (CrIS) (Shephard and Cady-Pereira, 2015), the Tropospheric Emission Spectrometer
87 (TES) (Shephard et al., 2015), and Greenhouse Gases Observing Satellite (Someya et al., 2020)
88 are publicly available. Most of them have been validated against ground-based observations or
89 complemented with other remote sensing products (Van Damme et al., 2015, 2018; Dammers
90 et al., 2016, 2017, 2019; Kharol et al., 2018; Shephard et al., 2020; Whitburn et al., 2016).

91 Accordingly, a few studies on ammonia emission calculations have been recently
92 published relying on 4D-Variational inversion schemes such as (Cao et al., 2022; Zhu et al.,
93 2013) or process based models (Beaudor et al., 2023; Vira et al., 2020). More recently, Sitwell
94 et al. (2022) proposed an inversion scheme for a non-linear CrIS observation model using
95 alternation between CrIS ammonia retrievals performed with the logarithm of concentrations
96 and linearized retrievals. In the present study, we use direct comparisons between the CrIS
97 observations and model retrievals using the Least Squares with Adaptive Prior Covariance (LS-
98 APC) algorithm (Tichý et al., 2016), which reduces the number of tuning parameters in the
99 method significantly using variational Bayesian approximation technique. We constrain
100 ammonia emissions over Europe over the 2013–2020 period and validate the results against
101 ground-based observations from EMEP (European Monitoring and Evaluation Programme,
102 <https://emep.int/mscw/>) (Torseth et al., 2012).

103 **2 Methods**

104 **2.1 CrIS observations**

105 To constrain ammonia emissions with inverse modelling, satellite measurements were
106 adopted from the Cross-Track Infrared Sounder (CrIS) onboard the NASA Suomi National
107 Polar-orbiting Partnership (S-NPP) satellite, which provides atmospheric soundings with a
108 spectral resolution of 0.625 cm^{-1} (Shephard et al., 2015). CrIS presents improved vertical
109 sensitivity for ammonia closer to the surface due to the low spectral noise in the ammonia
110 spectral region (Zavyalov et al., 2013) and the early afternoon overpass that typically coincides
111 with high thermal contrast, which is optimal for thermal infrared sensitivity. The CrIS Fast
112 Physical Retrieval (CFPR) (Shephard and Cady-Pereira, 2015) retrieves ammonia profiles at
113 14 levels using a physics-based optimal estimation retrieval, which also provides the vertical



114 sensitivity (averaging kernels) and an estimate of the retrieval errors (error covariance matrices)
115 for each measurement. As peak sensitivity typically occurs in the boundary layer between 900
116 and 700 hPa (~ 1 to 3 km) (Shephard et al., 2020) and the surface and total column
117 concentrations are both highly correlated with these boundary layer retrieved levels. The total
118 column random measurement error is estimated in the 10–15% range, with total random errors
119 estimates of ~30% (Shephard et al., 2020). The individual profile retrieval levels show an
120 estimated random measurement error of 10–30 %, with total random errors estimates increasing
121 to 60 to 100% due to the limited vertical resolution. These vertical sensitivity and error output
122 parameters are also useful for using CrIS observations in applications (e.g. data fusion, data
123 assimilation; model-based emission inversions; (Cao et al., 2020; Li et al., 2019)), as a satellite
124 observational operator can be generated in a robust manner. The detection limit of CrIS
125 measurements has been calculated down to 0.3–0.5 ppbv (Shephard et al., 2020). CrIS ammonia
126 has been evaluated against other observations over North America with the Ammonia
127 Monitoring Network (AMoN) (Kharol et al., 2018) and against ground-based Fourier transform
128 infrared (FTIR) spectroscopic observations (Dammers et al., 2017) showing small bias and high
129 correlations.

130 Daily CrIS ammonia (version 1.6.3) was interpolated onto a $0.5^\circ \times 0.5^\circ$ grid covering all
131 of Europe (10°W – 50°E , 25°N – 75°N) for the period 2013–2020. Interpolation was chosen due
132 to the large number of observations (around 10,000 per day per vertical level consisting of 2920
133 retrievals), which made the calculation of source-receptor matrices (SRMs) computationally
134 inefficient. Through interpolation we limited the number of observation (and thus the number
135 of SRMs to be calculated) to 12000 per day for 6 vertical levels. Sitwell et al. (2022) showed
136 that the averaging kernels of CrIS ammonia are significant only for the lowest six levels (the
137 upper eight have no influence onto the satellite observations) and therefore we considered only
138 these six vertical levels (~1018–619 hPa).

139 **2.2 A priori emissions of ammonia**

140 We used as a priori emissions for ammonia in the inversion algorithm the ones calculated
141 (i) from the most recent version of ECLIPSEv6 (Evaluating the CLimate and Air Quality
142 ImPacts of Short-livEd Pollutants) (Klimont, 2022; Klimont et al., 2017) combined with
143 biomass burning emissions from GFEDv4 (Global Fire Emission Dataset) (Giglio et al., 2013)
144 hereafter “EC6G4”, (ii) a more traditional dataset from ECLIPSEv5, GFED4 and GEIA (Global
145 Emissions InitiAtive), hereafter “EGG” (Bouwman et al., 1997; Giglio et al., 2013; Klimont et
146 al., 2017), (iii) emissions calculated from IASI (Infrared Atmospheric Sounding Interferometer)



147 and a 1-dimensional box-model and a modelled lifetime (Evangeliou et al., 2021), denoted as
148 “NE” and (iv) from the high resolution dataset of Van Damme et al. (2018) after applying a
149 simple 1-dimensional box-model (Evangeliou et al., 2021), hereafter denoted as “VD”. Given
150 the large uncertainty in ammonia emissions illustrated in Figure 1, we calculated the average
151 of these four priors (hereafter “avgEENV”) to establish the a priori emissions used in this study.

152 **2.3 Lagrangian particle dispersion model for the calculation of source-receptor** 153 **matrices (SRMs) of ammonia**

154 SRMs were calculated for each $0.5^\circ \times 0.5^\circ$ grid-cell over Europe (10°W – 50°E , 25°N –
155 75°N) using the Lagrangian particle dispersion model FLEXPART version 10.4 (Pisso et al.,
156 2019) adapted to simulate ammonia. The adaptation of the code includes treatment for the loss
157 processes of ammonia adopted from the Eulerian model LMDZ-OR-INCA (horizontal
158 resolution of $2.5^\circ \times 1.3^\circ$ and 39 hybrid vertical levels) that includes all atmospheric processes
159 and a state-of-the-art chemical scheme (Hauglustaine et al., 2004). The model accounts for
160 large-scale advection of tracers (Hourdin and Armengaud, 1999), deep convection (Emanuel,
161 1991), while turbulent mixing in the planetary boundary layer (PBL) is based on a local second-
162 order closure formalism. The model simulates atmospheric transport of natural and
163 anthropogenic aerosols and accounts for emissions, transport (resolved and sub-grid scale), and
164 dry and wet deposition. LMDZ-OR-INCA includes a simple chemical scheme for the ammonia
165 cycle and nitrate particle formation, as well as a state-of-the-art $\text{CH}_4/\text{NO}_x/\text{CO}/\text{NMHC}/\text{O}_3$
166 tropospheric photochemistry (Hauglustaine et al., 2014). To calculate chemical loss of
167 ammonia to $\text{PM}_{2.5}$, after a month of spin-up, global atmospheric transport of ammonia was
168 simulated for 2013–2020 by nudging the winds of the 6-hourly ERA Interim Reanalysis data
169 (Dee et al., 2011) with a relaxation time of 10 days (Hourdin et al., 2006). Using the EGG
170 inventory, we calculated the e-folding lifetime of ammonia in the model, which was adopted in
171 FLEXPART. We refer the reader to (Tichý et al., 2022) for a detailed description of the
172 formalism. Atmospheric linearities of the system and a full validation against ground-based
173 observation are also presented in the same paper.

174 FLEXPART releases computational particles that are tracked backward in time using
175 ERA5 (Hersbach et al., 2020) assimilated meteorological analyses from the European Centre
176 for Medium-Range Weather Forecasts (ECMWF) with 137 vertical layers, a horizontal
177 resolution of $0.5^\circ \times 0.5^\circ$ and a temporal hourly one. FLEXPART simulates turbulence (Cassiani
178 et al., 2014), unresolved mesoscale motions (Stohl et al., 2005) and includes a deep convection
179 scheme (Forster et al., 2007). SRMs were calculated for 7 days backward in time, at temporal



180 intervals that matched satellite measurements and at spatial resolution of $0.25^\circ \times 0.25^\circ$. This 7-
181 day backward tracking is sufficiently long to include almost all ammonia sources that contribute
182 to surface concentrations at the receptors given a typical atmospheric lifetime of about half a
183 day (Van Damme et al., 2018; Evangeliou et al., 2021).

184 **2.4 Inverse modeling algorithm**

185 The inversion method used in the present study relies on optimization of the distance
186 between the CrIS satellite vertical profile observations, denoted as v^{sat} , and retrieved vertical
187 profile, v^{ret} . The CrIS satellite retrieved observations are in situ profiles with an instrument
188 operator applied in logarithm space (Rodgers, 2000) as follows:

$$189 \quad \ln(v^{ret}) = \ln(v^a) + A(\ln(v^{true}) - \ln(v^a)) \quad (1)$$

190 where v^{ret} is the retrieved profile concentration vector, v^a is a priori profile concentration
191 vector used in the satellite retrievals, v^{true} is the hypothetical true profile concentration vector
192 supplied by the model ($v^{true} = v^{mod}$), and A is the averaging kernel matrix (for each
193 $0.5^\circ \times 0.5^\circ$ resolution grid-cell). This is a useful technique for evaluating if the retrieval
194 algorithm is performing as designed, i.e., it is unbiased and the root mean square error (RMSE)
195 is within the expected variability. The v^{mod} term can be written as:

$$196 \quad v^{mod} = Mx \quad (2)$$

197 for each grid-cell of the spatial domain, where M is the grid-cell specific SRM calculated with
198 FLEXPART and x is the unknown grid-cell specific emission vector. The SRM matrix M is
199 calculated on circular surroundings around each grid-cell due to computational effectiveness.
200 We select 4 degrees radius surroundings (approx. 445 kilometers) which is shown to be
201 sufficient for reliable emission estimation and low sensitivity has been observed with this
202 choice. Since the vector x is unknown, we replace it by a prior emission x^a (see section 2.2) in
203 the initial step that is gradually refined iteratively based on the satellite observations.

204 The used inversion setup is based on iterative minimization of distance between v^{sat} and
205 v^{ret} updating (iteratively) the emission x such as below:

$$206 \quad \arg \min_{x^a \rightarrow x} \|v^{sat} - v^{ret}\|_2^2 \quad (3)$$

207 for each grid-cell of computational domain. The minimization problem is solved in two steps.

208 First, we construct the linear inverse problem where v^{ret} from the given surroundings,
209 denoted here as S , forms the block-diagonal matrix v_S^{ret} while v^{sat} from the given
210 surroundings form an associated observation vector v_S^{sat} . This forms the linear inverse
211 problem:



212
$$v^{sat} = v_s^{ret} q_S \quad (4)$$

213 where the vector q_S is a vector with coefficients denoting how x^a needs to be refined to obtain
214 emission estimate vector x . We solve Eq. 4 using the least squares with adaptive prior
215 covariance (LS-APC) algorithm (Tichý et al., 2016). The algorithm is based on variational
216 Bayesian methodology assuming non-negative solution and favoring solution without abrupt
217 changes and it minimizes the use of manual tuning (Tichý et al., 2020).

218 Second, the grid-cell specific coefficient vector q_S is propagated in Eq. 1 to refine a prior
219 emission x^a and obtain estimated unknown emissions x . To maintain stability of the method,
220 we bound the ratio between prior and posterior emission elements to 0.01 and 100, respectively.
221 This choice, motivated by Cao et al. (2020), omits unrealistically small or high emissions,
222 however, the bounds are large enough to allow for new sources, as well as for attenuation of
223 old sources. For this reason, the choice of prior emission is of great importance in the method.

224 Note that CrIS data for some spatiotemporal elements are missing in the dataset. In these
225 cases, we interpolated the missing data following the method proposed by D’Errico (2023),
226 which solves a direct linear system of equations for NaN elements, while the extrapolation
227 behavior of the method is linear. Another strategy recently adopted in the literature has been to
228 tackle the missing data using total variation methodology (see details in Fang et al., 2023);
229 however, the method has been limited so far to its use on point-source release, hence we did
230 not use it in this work.

231 **3 Results**

232 **3.1 Emissions of ammonia in Europe (2013–2020)**

233 We analyze the CrIS ammonia satellite observations for Europe (10°W–50°E, 25°N–
234 75°N) over the 2013-2020 period on monthly basis to derive ammonia emissions using the
235 inverse modelling methodology described in Section 2.4. The inversion algorithm is applied to
236 each year of CrIS observations separately with the use of the avgEENV prior emission.

237 The overall resulting spatial distribution of the posterior emissions of ammonia (denoted
238 as posterior_avgEENV) averaged for the whole period are displayed in Figure 2 (top-left). The
239 highest emissions occur in Northwestern Europe (including Northern Belgium, the Netherlands
240 and northwestern Germany) and to a smaller extent in the Po Valley (Italy), and the Ebro Valley
241 (Spain). Local maxima are also seen over Pulawy (Poland), South Romania and Kutina
242 (Croatia) due to industrial applications (Clarisse et al., 2019; Van Damme et al., 2018). While
243 ammonia emissions were not calculated high in the Po Valley (8 year average), it has been



244 reported that in Lombardy, about 90% of the ammonia emissions there have been reported to
245 originate from manure management (Lonati and Cernuschi, 2020). The Ebro Valley is
246 characterized by intensive agricultural activities (Lassaletta et al., 2012; Lecina et al., 2010)
247 and the Aragon and Catalonia regions by large pig farms (Van Damme et al., 2022). Finally,
248 both Belgium and The Netherlands are countries in which intensive livestock activity is
249 documented. It consists mostly of dairy cow, beef cattle, pig and chicken farming (Gilbert et
250 al., 2018; Lesschen et al., 2011; Velthof et al., 2012).

251 Figure 2 (top-right) shows the annual posterior emissions discretized monthly for the
252 whole period (solid line) compared to prior ammonia emissions (dashed line). Higher emissions
253 than the prior ones were calculated, which is not necessarily attributed to emission increases
254 over Europe, but rather to miscalculation of emissions in the prior bottom-up inventories that
255 were used. A strong seasonal cycle is also observed peaking in the middle of each year
256 (summer) of the study period, but for several of these years, the characteristic bimodal cycle
257 also appears with another peak in spring (Beaudor et al., 2023).

258 To examine more closely the seasonal variability of ammonia emissions in Europe, we
259 present the monthly posterior emissions of ammonia averaged for the whole study period
260 (2013–2020) at the bottom-left panel of Figure 2 together with the prior ones. The interannual
261 variability over the period between 2013 and 2020, is also apparent in the monthly box and
262 whisker plots of the posterior emissions. In addition, the spatial distribution of monthly
263 ammonia emissions averaged for the eight-year period is given in Supplementary Figure S 1. It
264 appears that ammonia emissions are very low in wintertime (DJF average: 286 Gg) over Europe
265 and increase towards summer (JJA average: 563 Gg), due to temperature dependent
266 volatilization of ammonia (Sutton et al., 2013), with the largest emissions occurring in August
267 (601 Gg). Although a clear peak of fertilization in early spring is missing from the plot,
268 emissions start to increase in early spring to peak in late-summer (Van Damme et al., 2022)
269 corresponding to the start and end of the fertilization periods in Europe (Paulot et al., 2014).
270 Fertilization is tightly regulated in Europe (Ge et al., 2020). It is only allowed from February
271 to mid-September in The Netherlands, while manure application is also only allowed during
272 the same period depending on the type of manure and the type of land (Van Damme et al.,
273 2022). In Belgium, nitrogen fertilizers are only allowed from mid-February to the end of August
274 (Van Damme et al., 2022), so as in Germany (restricted in winter months) (Kuhn, 2017).

275 Finally, Figure 2 (bottom-right) shows the annual posterior emissions for the whole
276 period with the annual total emissions for each year. We observe a significant decrease in
277 ammonia posterior emissions over Europe during the 2013–2020 period. Emissions were



278 estimated as 5431 Gg for 2013 decreasing to 4890 Gg in 2014. A minor increase can be seen
279 in 2015 (5104 Gg), after which a significant decrease of 534 Gg (more than 10%) was estimated,
280 followed by the nearly constant plateau at the levels between 4383 Gg in 2017, 4323 Gg in
281 2019 and finally to 3994 Gg in 2020. The gradual decrease in ammonia emissions over Europe
282 since 2013 is also plotted spatially in Supplementary Figure S 2. It is evident that the restrictions
283 and measures adopted by the European Union to reduce secondary PM formation were
284 successful, as emissions in the hot-spot regions of Belgium, The Netherlands, Germany and
285 Poland declined drastically over time. However, an increase of +4.4% was observed in 2015. It
286 has been reported that ammonia emissions increased in 2015 and several European Union
287 Member States, as well as the EU as a whole, exceeded their respective ammonia emission
288 ceilings (EEA, 2017). The increase was reported to be +1.8% and was mainly caused by
289 increased emissions in Germany, Spain, France, and the United Kingdom. This was caused by
290 extensive use of inorganic nitrogen fertilizers (including urea application) in Germany, while
291 increased emissions in Spain were driven by an increase in the consumption of synthetic
292 nitrogen fertilizers and in the number of cattle and pigs (EEA, 2017). It should be mentioned
293 that a partial decrease of ammonia in 2020 might be due to the COVID-19 pandemic, mainly
294 due to bias created by the decrease of NO_x and SO₂ that are precursor species of the atmospheric
295 acids, with which ammonia reacts (see Tichý et al., 2022).

296 **3.2 Country by country ammonia emissions**

297 Posterior annual emissions of ammonia for 2013–2020 are plotted for four European
298 regions (Western, Central and Eastern, Northern and Southern Europe) in the left panel of
299 Figure 3, while the estimated seasonal variation of each region is shown on the right panels
300 averaged over the whole eight-year period. Western Europe includes Ireland, Austria, France,
301 Germany, Belgium, Andorra, Luxembourg, The Netherlands, Switzerland, and United
302 Kingdom; Central and Eastern Europe include Albania, Bosnia and Herzegovina, Bulgaria,
303 Czechia, Croatia, Hungary, Belarus, Slovakia, North Macedonia, Montenegro, Poland,
304 Romania, Moldova, Slovenia, Ukraine, and Serbia; Northern Europe is defined by Denmark,
305 Estonia, Finland, Latvia, Lithuania, Faroe Islands, Norway, and Sweden; finally, Southern
306 Europe includes Cyprus, Greece, Italy, Portugal, Spain.

307 The most significant decreases in ammonia emissions were estimated to be -38% in
308 Central and Eastern Europe and -37% in Western Europe, respectively. Quantitatively, Central
309 and Eastern Europe emissions were estimated to gradually drop from 2190 Gg in 2013 and to
310 1495 Gg in 2020 with a small increase in 2015 (2171 Gg) mainly because Germany, France



311 and the United Kingdom missed their emission targets (EEA, 2017). Western European
312 emissions of ammonia also declined constantly over time from 2041 Gg in 2013 to 1421 Gg in
313 2020. Smaller, yet significant, decreases were calculated over Northern Europe from 398 Gg in
314 2013 to 333 Gg in 2020 (-17%). Finally, Southern Europe exhibited a minor drop between years
315 2013 and 2014 (from 803 Gg in 2013 to 729 Gg in 2014) followed by a small increase until
316 2019 (from 729 to 803 Gg), and then decreased again in 2020 to 743 Gg. Overall, Southern
317 European emissions decreased by -7.62%.

318 The seasonal cycle of ammonia was again characterized by the restrictions applied to the
319 agricultural-related activities by the European Union member states (Figure 3, right panels). As
320 such, emissions in Western, Central and Eastern and Southern Europe were very low in winter
321 and started increasing when fertilization was allowed in early spring, whereas the increasing
322 temperature towards summer increased volatilization and, thus, emissions of ammonia (Van
323 Damme et al., 2022; Ge et al., 2020). Although much less marked than in other European
324 regions due to lower prevailing temperatures and weaker agricultural applications, emissions
325 in Northern Europe show the spring-summer temperature dependence. However, emissions
326 were estimated to be double in winter rather following the cycle of SO₂ (Tang et al., 2020).
327 Despite measurements have shown that ammonia might increase in winter at high latitudes (Aas
328 et al., 2020), we conclude that the model likely underperforms here. Supplementary Figure S 3
329 shows prior emissions in Western, Central and Eastern, Northern and Southern Europe for
330 EC6G4 and NE emission inventories. Both show the aforementioned increase in emissions
331 during winter in Northeastern Europe. Especially the NE emissions dominate the a priori
332 emissions that were used here (avgEENV), because they are the highest, whereas the winter
333 peak in the north is extreme (emissions decline from 35 to 12 Gg). Therefore, there is a very
334 strong dependence of the posterior seasonality of ammonia in Northern Europe due to the strong
335 prior that we use there.

336 Country specific emissions of posterior ammonia on a monthly basis (eight-year average
337 emissions) are shown for 20 countries in Supplementary Figure S 4. For countries such as
338 Portugal, Spain, Italy, United Kingdom, The Netherlands, Belgium, Poland, Hungary,
339 Denmark, Belarus and Romania two peaks can be clearly seen in late spring and end of summer.
340 As discussed before, these peaks coincide with the two main fertilization periods in Europe
341 (Paulot et al., 2014). However, it is expected that ammonia abundance is high throughout the
342 entire spring–summer period (e.g., Greece, France, Germany, Czechia, Ukraine and Bulgaria)
343 due to agricultural activity and temperature dependent volatilization (Sutton et al., 2013).



344 Ammonia emissions in Finland, Sweden and Norway are smaller than in the rest of Europe and
345 show a reverse seasonality.

346 **3.3 Uncertainties in ammonia's posterior emissions**

347 For the calculation of uncertainty of posterior emissions of ammonia, we benefit from the
348 form of posterior, which arises as a Gaussian distribution with calculated mean and standard
349 deviation for each element of our spatiotemporal domain. In accordance with the posterior
350 emissions defined in Section 2.4, we propagate the standard deviation through Eq. 1 to obtain
351 the uncertainty of each spatiotemporal element, here denoted as $u_{\text{elem},t}$. If two variables follow
352 a Gaussian distribution with means μ_1 and μ_2 and standard deviations σ_1 and σ_2 , the sum of
353 these variables has the mean $\mu_1 + \mu_2$ and standard deviation $\sqrt{\sigma_1^2 + \sigma_2^2}$. Therefore, the total
354 uncertainty for each spatial element over the temporal axis is then a square root of summed
355 uncertainties over the selected time steps $[t_1; t_2]$:

$$356 \quad U_{\text{elem}} = \sqrt{\sum_{t=t_1}^{t_2} u_{\text{elem},t}^2} \quad (5)$$

357 The calculated posterior uncertainty for our spatial domain and studied period (2013–
358 2020) is shown in Figure 5. Here, we display uncertainty calculated as 2 standard deviations (2
359 σ), i.e. 95% of the values lay inside the interval with the center in the reported emission
360 surrounded by the reported uncertainty. The same results for each year of the study period are
361 depicted in Supplementary Figure S 5. The absolute uncertainty of posterior ammonia
362 emissions reaches a maximum of 25 ng m⁻² s⁻¹ or about 42% (relative value). In general, the
363 pattern of posterior uncertainty follows the one of the posterior emissions, with the highest
364 values over (i) Belgium, the Netherlands, and Germany due to livestock, farming, and
365 agricultural activity; (ii) Poland, South Romania and Croatia due to industrial applications; (iii)
366 Catalonia due to pig farming; (iv) West France due to manure application. Nevertheless, the
367 obtained posterior uncertainty remains low, and this depicts the robustness of the methodology
368 used and the calculated posterior emissions of ammonia.

369 **3.4 Validation of posterior emissions**

370 As shown in Eq. 3 (Section 2.4), the inversion algorithm minimizes the distance between
371 the satellite observations (v^{sat}) and the retrieved ammonia concentrations (v^{ret}). The latter is
372 a function of different satellite parameters (e.g., averaging kernel sensitivities) and modelled
373 ammonia concentrations using a prior dataset (v^{mod} or v^{true}) as seen in Eq. 1. The overall
374 result is always propagated to v^{mod} iteratively, each time updating the prior emissions to obtain



375 posterior ammonia. As specified in CrIS guidelines, modelled concentrations (v^{mod}) cannot be
 376 directly compared with satellite data (v^{sat}), while comparing v^{sat} with v^{ret} is not a proper
 377 validation method, because the comparison is performed for satellite observations that were
 378 included in the inversion (dependent observations), and the inversion algorithm has been
 379 designed to reduce the $v^{sat}-v^{ret}$ mismatches. This means that the reduction of the posterior
 380 retrieved concentration (v^{ret}) mismatches to the observations (v^{sat}) is determined by the
 381 weighting that is given to the observations with respect to v^{ret} . A proper validation of the
 382 posterior emissions is performed against observations that were not included in the inversion
 383 (independent observations).

384 For these reasons, we compare modelled posterior concentrations of ammonia (v^{mod}) at
 385 the surface with ground-based observations over Europe from the EMEP (European Monitoring
 386 and Evaluation Programme, <https://emep.int/mscw/>) network (Torseth et al., 2012). The
 387 measurements are open in public and can be retrieved from <https://ebas.nilu.no>. We used
 388 measurements for all years between 2013 and 2020 from an average of 53 stations with 2928
 389 observations for each station covering all Europe (Supplementary Figure S 6). The comparison
 390 is plotted for each of the 53 stations separately on a Taylor diagram in Figure 6. For all stations,
 391 the Pearson's correlation coefficient increased for the posterior ammonia (coloured circles)
 392 increased as compared to the prior one (coloured squares) reaching above 0.6 at several stations,
 393 while the normalized root mean square error (nRMSE) and standard deviation were kept below
 394 2 (unitless) and 2 $\mu\text{g m}^{-3}$, respectively, in almost all stations (except SI0008 in Slovenia).

395 To further show how posterior emissions of ammonia affect modelled concentrations, we
 396 chose six stations (DE0002 in Germany, NO0056 in South Norway, ES0009 in Spain, NL0091
 397 in the Netherlands, HU0002 in Hungary and PL0005 in Poland) from the EMEP network
 398 (highlighted in red in Supplementary Figure S 6), and we plot prior and posterior concentrations
 399 against ground-based ammonia over time for the whole study period (2013–2020) in
 400 Supplementary Figure S 7. Given the long period of plotting, we average observations every
 401 week and modelled concentrations every month for a more visible representation of the
 402 comparison. To evaluate the comparison, we calculate a number of statistic measures, namely
 403 nRMSE, the normalized mean absolute error (nMAE) and the root mean squared logarithmic
 404 error (RMSLE) as defined below:

$$\begin{aligned}
 405 \quad nRMSE &= \sqrt{\frac{\sum_{i=1}^n \frac{1}{n} (m_i - o_i)^2}{\frac{1}{n} \sum_{i=1}^n o_i}} & nMAE &= \frac{\sum_{i=1}^n |m_i - o_i|}{\sum_{i=1}^n o_i} \\
 406 \quad RMSLE &= \sqrt{\frac{1}{n} \sum_{i=1}^n (\log m_i - \log o_i)^2} & (6)
 \end{aligned}$$



407 where n is sample size, m and o the individual sample points for model concentrations and
408 observations of ammonia indexed with i . As one can see in Supplementary Figure S 7, all
409 statistics were improved in all six stations and posterior concentrations were closer to the
410 observations. However, individual peaks were in many cases misrepresented in the model.
411 Whether this is a result of the measurement technique or the fact that local sources cannot be
412 considered for such high spatiotemporal resolution as those in the CTM and FLEXPART (given
413 the short lifetime of atmospheric ammonia) needs further research. The best results were
414 obtained at station ES0009 (Spain), where model captures the seasonal variation of the
415 observations during the whole study period (2013–2020). In all other stations, the seasonality
416 is maintained albeit steep peaks in the observations are lost.

417 **4 Discussion**

418 We compared our posterior estimates with two recently published studies on ammonia
419 emission in Europe (Cao et al., 2022; Luo et al., 2022). Luo et al. (2022) used IASI observations
420 for the period 2008 to 2018 to estimate ammonia emissions in a global domain. Their method
421 was based on updating prior emissions with correction term computed using differences
422 between observed and simulated ammonia columns combined with calculated ammonia
423 lifetimes. The key indicators calculated for the European domain in Luo et al. (2022) are a
424 linear trend for the 2008–2018 period, average annual emissions, and relative trends. Note that
425 we compare our eight-year period with a decade in Luo et al. (2022). The comparison is
426 depicted in Figure 4. Our estimates (Figure 4, left panel) are in good agreement with those
427 calculated by Luo et al. (2022). The linear trend was estimated as -1.27 Tg for the period by
428 Luo et al. (2022), while our estimate is -1.44 Tg. The spatial distribution of the trend is also
429 given in Figure 4 (left panel). The key decrease is observed mainly in France, Germany, and
430 middle Europe, while the increasing trend is observed mostly in Spain, parts of Italy, and
431 Greece. The average annual ammonia emission for the European domain in Luo et al. (2022)
432 was estimated to be 5.05 Tg while our estimate is 4.63 Tg. Our lower estimate (by
433 approximately 8%) may be attributed to use of more recent period considered in our study, but
434 both methods agree that the trend in Europe is negative. The relative decrease estimated by Luo
435 et al. (2022) is -25.1% , while we calculate -31.02% , which is again in very good agreement.

436 Cao et al. (2022) used CrIS observations for the year 2016 in order to estimate ammonia
437 emissions for 25 European Union members (EU25), namely Austria, Belgium, Bulgaria,
438 Croatia, Republic of Cyprus, Czech Republic, Denmark, Estonia, France, Germany, Greece,
439 Hungary, Ireland, Italy, Latvia, Lithuania, Luxembourg, Malta, Netherlands, Poland, Portugal,



440 Romania, Slovakia, Slovenia, and Spain. The method was tested with uni-directional and bi-
441 directional flux schemes. The uni-directional dry deposition scheme assumes only air to surface
442 exchange of ammonia ignoring changes in environmental conditions, while the bi-directional
443 scheme captures dynamics in measured ammonia fluxes. Total estimated ammonia emissions
444 for the EU25 region by the uni-directional scheme (posterior_uni) and the bi-directional scheme
445 (posterior_bi) were reported as 3534 Gg N y⁻¹ and 2850 Gg N y⁻¹, respectively. The
446 posterior_bi estimate is very close to our estimate for EU25 for the year 2016, which is 2712
447 Gg N y⁻¹, while the posterior_uni is approximately 30% higher. A uni-directional dry
448 deposition scheme treats surface exchange of ammonia between the atmosphere and biosphere
449 in a one-way manner (from air to surface) and ignores the impacts of changes in environmental
450 conditions (e.g., soil temperature, soil wetness, soil pH, fertilized condition, and vegetation
451 type) on ammonia emissions from fertilized soil and crops (volatilization), which likely lead to
452 high biases in top-down estimates. Ammonia in LMDz-OR-INCA model, that was used to
453 capture ammonia's losses, resembles a partially bi-directional treatment, where emissions and
454 deposition are both possible at the same time without any use of a compensation point; this may
455 explain the 30% difference.

456 The detailed EU25 emissions for the year 2016 are displayed in Figure 4 (right panel) for
457 posterior_uni (red), posterior_bi (yellow), our post_avgEENV (blue), and priors used by Cao
458 et al. (2022) and in our study (dashed red and blue, respectively). As seen from Figure 4, our
459 posterior estimates (post_avgEENV) have more similar characteristics with posterior_bi, with
460 monthly difference to be less than factor of 2 positive or negative from Cao et al. (2022). Note
461 that the posterior_uni estimates are always a factor of 3 higher than our posterior estimates for
462 ammonia emissions. The main differences can be observed during February-March and
463 October-November periods where our estimates are generally lower than those from Cao et al.
464 (2022).

465 5 Conclusions

466 Today, a large debate takes place about ammonia abatement strategies for Europe, but
467 also for Southeastern Asia, in an effort to reduce secondary formation and, thus, mitigate
468 climate crisis (van Vuuren et al., 2015). These strategies include (a) low nitrogen feed by
469 reducing ammonia emissions at many stages of manure management, from excretion in
470 housing, through storage of manure to application on land, also having positive effects on
471 animal health and indoor climate (Montalvo et al., 2015); (b) low emission livestock housing,
472 which focuses on reducing the surface and time manure is exposed to air by adopting rules and



473 regulations regarding new livestock houses (Poteko et al., 2019); (c) air purification by
474 adopting technologies to clean exhaust air from livestock buildings (Cao et al., 2023) and
475 others. Here, we examine the impact of such strategies adopted by several European countries
476 on the emissions of ammonia inferred using satellite observations from CrIS and a novel
477 inverse modelling algorithm. We examine and assess the changes on ammonia emissions for
478 the period 2013–2020. The main key messages can be summarized below:

- 479 • The highest emissions during the 2013–2020 study period occur in North Europe (Belgium,
480 the Netherlands and northwestern Germany). At a regional scale, peaks are seen in Western
481 Europe (Poland, South Romania and Croatia) due to industrial applications, in Spain (Ebro
482 Valley, Aragon, Catalonia) due to agricultural activities and farming, in Belgium and The
483 Netherlands due to livestock activity (dairy cow, beef cattle, pig and chicken farming).
- 484 • Ammonia emissions are low in winter (average: 286 Gg) and peak in summer (average:
485 563 Gg), due to temperature dependent volatilization of ammonia, while a notable peak
486 attributed to fertilization can be seen in early spring during some years.
- 487 • Over the 2013–2020 period, European emissions of ammonia decreased from 5431 Gg in
488 2013 to 3994 Gg in 2020 or about -26%. Hence, the restrictions adopted by the European
489 Union members were effective in reducing secondary PM formation.
- 490 • A slight emission increase of +4.4% in 2015 appears for several European Union Member
491 States (Germany, Spain, France, and the United Kingdom) who exceeded the respective
492 ammonia emission targets. Part of the 2020 ammonia decrease might be attributable to the
493 COVID-19 pandemic restrictions.
- 494 • The largest decreases in ammonia emissions were observed in Central and Eastern Europe
495 (-38%, 2190 Gg in 2013 to 1495 Gg in 2020) and in Western Europe (-37%, 2041 Gg in
496 2013 to 1421 Gg in 2020). Smaller decreases were calculated in Northern Europe (-17%,
497 398 Gg in 2013 to 333 Gg in 2020) and, Southern Europe (-7.6%, from 803 Gg in 2013 to
498 to 743 Gg in 2020).
- 499 • The maximum calculated absolute uncertainty of posterior emissions was $25 \text{ ng m}^{-2} \text{ s}^{-1}$, or
500 about 42% (relative value) following the spatial distribution of the posterior emissions.
- 501 • Comparison of the concentrations calculated with prior and posterior ammonia emissions
502 against independent (not used in the inversion algorithm) observations showed improved
503 correlation coefficients and low nRMSEs and standard deviations. Looking at timeseries
504 of six randomly selected stations in Europe, we also found that posterior surface



505 concentrations of ammonia were in accordance with the ground-based measurement, also
506 following the observed seasonal trends.

- 507 • Our results agree very well with those from Luo et al. (2022) (decreasing trend: -1.44
508 versus -1.27 Tg, annual European emissions: 4.63 versus 5.05 Tg) and those from Cao et
509 al. (2022) following their methodology (their posterior_{bi} estimate for EU25 and year 2016
510 was 2850 Gg N y⁻¹, while we calculate 2712 Gg N y⁻¹).
- 511 • The relatively low posterior uncertainty and improved statistics in the validation of the
512 posterior surface concentrations denote the robustness of the posterior emissions of
513 ammonia calculated with satellite measurements and our adapted inverse framework.

514

515 *Data availability.* The data generated for the present paper can be downloaded from ZENODO
516 (<https://doi.org/10.5281/zenodo.7646462>). FLEXPARTv10.4 is open access and can be
517 downloaded from <https://www.flexpart.eu/downloads>, while use of ERA5 data is free of
518 charge, worldwide, non-exclusive, royalty-free and perpetual. The inversion algorithm LS-APC
519 is open access from https://www.utia.cas.cz/linear_inversion_methods. CrIS ammonia can be
520 obtained by request to Dr. M. Shephard (Mark.Shephard@ec.gc.ca). EMEP measurements are
521 open in <https://ebas.nilu.no>. FLEXPART SRMs for 2013–2020 can be obtained from the
522 corresponding author upon request.

523

524 *Competing interests.* The authors declare no competing interests.

525

526 *Acknowledgements.* This study was supported by the Research Council of Norway (project
527 ID: 275407, COMBAT – Quantification of Global Ammonia Sources constrained by a
528 Bayesian Inversion Technique). We kindly acknowledge Dr. M. Shephard for providing CrIS
529 ammonia. This work was granted access to the HPC resources of TGCC under the allocation
530 A0130102201 made by GENCI (Grand Equipement National de Calcul Intensif).

531

532

533 *Author contributions.* O.T. adapted the inversion algorithm, performed the calculations,
534 analyses and wrote the paper. S.E. adapted FLEXPARTv10.4 to model ammonia chemical loss.
535 Y.B. and D.H. set up the CTM model and performed the simulation, the output of which was
536 used as input in FLEXPART. N.E. performed the FLEXPART simulations, contributed to
537 analyses, wrote and coordinated the paper. All authors contributed to the final version of the
538 manuscript.



539

540 **References**

- 541 Aas, W., Eckhardt, S., Fiebig, M., Platt, S. M., Solberg, S., Yttri, K. E. and Zwaafink,
542 C. G.: Monitoring of long-range transported air pollutants in Norway., 2020.
- 543 Abbatt, J. P. D., Benz, S., Cziczo, D. J., Kanji, Z., Lohmann, U. and Mohler, O.: Solid
544 Ammonium Sulfate Aerosols as Ice Nuclei: A Pathway for Cirrus Cloud Formation,
545 *Science* (80-.), 313(September), 1770–1773, 2006.
- 546 Beaudor, M., Vuichard, N., Lathi re, J., Evangelidou, N., Damme, M. Van, Clarisse, L.
547 and Hauglustaine, D.: Global agricultural ammonia emissions simulated with the
548 ORCHIDEE land surface model, *Geosci. Model Dev.*, 16, 1053–1081 [online]
549 Available from: <https://doi.org/10.5194/egusphere-2022-626>, 2023.
- 550 Behera, S. N., Sharma, M., Aneja, V. P. and Balasubramanian, R.: Ammonia in the
551 atmosphere: A review on emission sources, atmospheric chemistry and deposition
552 on terrestrial bodies, *Environ. Sci. Pollut. Res.*, 20(11), 8092–8131,
553 doi:10.1007/s11356-013-2051-9, 2013.
- 554 Bouwman, A. F., Lee, D. S., Asman, W. A. H., Dentener, F. J., Van Der Hoek, K. W.
555 and Olivier, J. G. J.: A global high-resolution emission inventory for ammonia, *Global*
556 *Biogeochem. Cycles*, 11(4), 561–587, doi:10.1029/97GB02266, 1997.
- 557 Cao, H., Henze, D. K., Shephard, M. W., Dammers, E., Cady-Pereira, K., Alvarado,
558 M., Lonsdale, C., Luo, G., Yu, F., Zhu, L., Danielson, C. G. and Edgerton, E. S.:
559 Inverse modeling of NH₃ sources using CrIS remote sensing measurements,
560 *Environ. Res. Lett.*, 15, 104082, doi:10.1088/1748-9326/abb5cc, 2020.
- 561 Cao, H., Henze, D. K., Zhu, L., Shephard, M. W., Cady-Pereira, K., Dammers, E.,
562 Sitwell, M., Heath, N., Lonsdale, C., Bash, J. O., Miyazaki, K., Flechard, C., Fauvel,
563 Y., Kruit, R. W., Feigenspan, S., Br mmer, C., Schrader, F., Twigg, M. M., Leeson,
564 S., Tang, Y. S., Stephens, A. C. M., Braban, C., Vincent, K., Meier, M., Seidler, E.,
565 Geels, C., Ellermann, T., Sanocka, A. and Capps, S. L.: 4D-Var Inversion of
566 European NH₃ Emissions Using CrIS NH₃ Measurements and GEOS-Chem Adjoint
567 With Bi-Directional and Uni-Directional Flux Schemes, *J. Geophys. Res. Atmos.*,
568 127(9), 1–25, doi:10.1029/2021JD035687, 2022.
- 569 Cao, T., Zheng, Y., Dong, H., Wang, S., Zhang, Y. and Cong, Q.: A new air cleaning
570 technology to synergistically reduce odor and bioaerosol emissions from livestock
571 houses, *Agric. Ecosyst. Environ.*, 342(October 2022), 108221,
572 doi:10.1016/j.agee.2022.108221, 2023.
- 573 Cassiani, M., Stohl, A. and Brioude, J.: Lagrangian Stochastic Modelling of
574 Dispersion in the Convective Boundary Layer with Skewed Turbulence Conditions
575 and a Vertical Density Gradient: Formulation and Implementation in the FLEXPART
576 Model, *Boundary-Layer Meteorol.*, 154(3), 367–390, doi:10.1007/s10546-014-9976-
577 5, 2014.
- 578 Clarisse, L., Van Damme, M., Clerbaux, C. and Coheur, P. F.: Tracking down global
579 NH₃ point sources with wind-adjusted superresolution, *Atmos. Meas. Tech.*, 12(10),
580 5457–5473, doi:10.5194/amt-12-5457-2019, 2019.
- 581 Crippa, M., Solazzo, E., Huang, G., Guizzardi, D., Koffi, E., Muntean, M., Schieberle,
582 C., Friedrich, R. and Janssens-Maenhout, G.: High resolution temporal profiles in the
583 Emissions Database for Global Atmospheric Research, *Sci. Data*, 7(1), 1–17,
584 doi:10.1038/s41597-020-0462-2, 2020.
- 585 D'Errico, J.: Inpaint_nans, [online] Available from:
586 https://www.mathworks.com/matlabcentral/fileexchange/4551-inpaint_nans, 2023.
- 587 Van Damme, M., Clarisse, L., Dammers, E., Liu, X., Nowak, J. B., Clerbaux, C.,
588 Flechard, C. R., Galy-Lacaux, C., Xu, W., Neuman, J. A., Tang, Y. S., Sutton, M. A.,



- 589 Erisman, J. W. and Coheur, P. F.: Towards validation of ammonia (NH₃)
590 measurements from the IASI satellite, *Atmos. Meas. Tech.*, 8(3), 1575–1591,
591 doi:10.5194/amt-8-1575-2015, 2015.
- 592 Van Damme, M., Whitburn, S., Clarisse, L., Clerbaux, C., Hurtmans, D. and Coheur,
593 P.: Version 2 of the IASI NH₃ neural network retrieval algorithm : near-real-time and
594 reanalysed datasets, *Atmos. Meas. Tech.*, 10, 4905–4914, 2017.
- 595 Van Damme, M., Clarisse, L., Whitburn, S., Hadji-Lazaro, J., Hurtmans, D., Clerbaux,
596 C. and Coheur, P. F.: Industrial and agricultural ammonia point sources exposed,
597 *Nature*, 564(7734), 99–103, doi:10.1038/s41586-018-0747-1, 2018.
- 598 Van Damme, M., Clarisse, L., Stavrakou, T., Wichink Kruit, R., Sellekaerts, L., Viatte,
599 C., Clerbaux, C. and Coheur, P. F.: On the weekly cycle of atmospheric ammonia
600 over European agricultural hotspots, *Sci. Rep.*, 12(1), 1–9, doi:10.1038/s41598-022-
601 15836-w, 2022.
- 602 Dammers, E., Palm, M., Van Damme, M., Vigouroux, C., Smale, D., Conway, S.,
603 Toon, G. C., Jones, N., Nussbaumer, E., Warneke, T., Petri, C., Clarisse, L.,
604 Clerbaux, C., Hermans, C., Lutsch, E., Strong, K., Hannigan, J. W., Nakajima, H.,
605 Morino, I., Herrera, B., Stremme, W., Grutter, M., Schaap, M., Kruit, R. J. W., Notholt,
606 J., Coheur, P. F. and Erisman, J. W.: An evaluation of IASI-NH₃ with ground-based
607 Fourier transform infrared spectroscopy measurements, *Atmos. Chem. Phys.*,
608 16(16), 10351–10368, doi:10.5194/acp-16-10351-2016, 2016.
- 609 Dammers, E., Shephard, M. W., Palm, M., Cady-pereira, K., Capps, S., Lutsch, E.,
610 Strong, K., Hannigan, J. W., Ortega, I., Toon, G. C., Stremme, W. and Grutter, M.:
611 Validation of the CrIS fast physical NH₃ retrieval with ground-based FTIR, *Atmos.*
612 *Meas. Tech.*, 87, 2645–2667, 2017.
- 613 Dammers, E., McLinden, C. A., Griffin, D., Shephard, M. W., Van Der Graaf, S.,
614 Lutsch, E., Schaap, M., Gainairu-Matz, Y., Fioletov, V., Van Damme, M., Whitburn,
615 S., Clarisse, L., Cady-Pereira, K., Clerbaux, C., Francois Coheur, P. and Erisman, J.
616 W.: NH₃ emissions from large point sources derived from CrIS and IASI satellite
617 observations, *Atmos. Chem. Phys.*, 19(19), 12261–12293, doi:10.5194/acp-19-
618 12261-2019, 2019.
- 619 Dee, D. P., Uppala, S. M., Simmons, A. J., Berrisford, P., Poli, P., Kobayashi, S.,
620 Andrae, U., Balmaseda, M. A., Balsamo, G., Bauer, P., Bechtold, P., Beljaars, A. C.
621 M., van de Berg, L., Bidlot, J., Bormann, N., Delsol, C., Dragani, R., Fuentes, M.,
622 Geer, A. J., Haimberger, L., Healy, S. B., Hersbach, H., H^{??}lm, E. V., Isaksen, L.,
623 K^{??}llberg, P., K^{??}hler, M., Matricardi, M., Mcnally, A. P., Monge-Sanz, B. M.,
624 Morcrette, J. J., Park, B. K., Peubey, C., de Rosnay, P., Tavolato, C., Th^{??}paut, J. N.
625 and Vitart, F.: The ERA-Interim reanalysis: Configuration and performance of the
626 data assimilation system, *Q. J. R. Meteorol. Soc.*, 137(656), 553–597,
627 doi:10.1002/qj.828, 2011.
- 628 EEA: European Union emission inventory report 1990 –2015 under the UNECE
629 Convention on Long-range Transboundary Air Pollution. [online] Available from:
630 <https://www.eea.europa.eu/publications/annual-eu-emissions-inventory-report>, 2017.
- 631 Emanuel, K. A.: A Scheme for Representing Cumulus Convection in Large-Scale
632 Models, *J. Atmos. Sci.*, 48(21), 2313–2329, doi:10.1175/1520-
633 0469(1991)048<2313:ASFRCC>2.0.CO;2, 1991.
- 634 Erisman, J. W., Bleeker, A., Galloway, J. and Sutton, M. S.: Reduced nitrogen in
635 ecology and the environment, *Environ. Pollut.*, 150(1), 140–149,
636 doi:10.1016/j.envpol.2007.06.033, 2007.
- 637 Evangeliou, N., Balkanski, Y., Eckhardt, S., Cozic, A., Van Damme, M., Coheur, P.-
638 F., Clarisse, L., Shephard, M., Cady-Pereira, K. and Hauglustaine, D.: 10–Year



- 639 Satellite-Constrained Fluxes of Ammonia Improve Performance of Chemistry
640 Transport Models, *Atmos. Chem. Phys.*, 21, 4431–4451, doi:10.5194/acp-21-4431-
641 2021, 2021.
- 642 Fang, S., Dong, X., Zhuang, S., Tian, Z., Zhao, Y., Liu, Y., Liu, Y. and Sheng, L.:
643 Inversion of 137Cs emissions following the Fukushima accident with adaptive release
644 recovery for temporal absences of observations, *Environ. Pollut.*, 317(September
645 2022), 120814, doi:10.1016/j.envpol.2022.120814, 2023.
- 646 Forster, C., Stohl, A. and Seibert, P.: Parameterization of convective transport in a
647 Lagrangian particle dispersion model and its evaluation, *J. Appl. Meteorol. Climatol.*,
648 46(4), 403–422, doi:10.1175/JAM2470.1, 2007.
- 649 Fowler, D., Muller, J. B. A., Smith, R. I., Dragosits, U., Skiba, U., Sutton, M. A. and
650 Brimblecombe, P.: A CHRONOLOGY OF NITROGEN DEPOSITION IN THE UK,
651 *Water, Air, Soil Pollut. Focus*, 4, 9–23, 2004.
- 652 Galloway, J. N., Aber, J. D., Erisman, J. A. N. W., Seitzinger, S. P., Howarth, R. W.,
653 Cowling, E. B. and Cosby, B. J.: The Nitrogen Cascade, *Bioscience*, 53(4), 341–356,
654 doi:10.1641/0006-3568(2003)053[0341:TNC]2.0.CO;2, 2003.
- 655 Ge, X., Schaap, M., Kranenburg, R., Segers, A., Jan Reinds, G., Kros, H. and De
656 Vries, W.: Modeling atmospheric ammonia using agricultural emissions with
657 improved spatial variability and temporal dynamics, *Atmos. Chem. Phys.*, 20(24),
658 16055–16087, doi:10.5194/acp-20-16055-2020, 2020.
- 659 Giannakis, E., Kushta, J., Bruggeman, A. and Lelieveld, J.: Costs and benefits of
660 agricultural ammonia emission abatement options for compliance with European air
661 quality regulations, *Environ. Sci. Eur.*, 31(1), doi:10.1186/s12302-019-0275-0, 2019.
- 662 Giglio, L., Randerson, J. T. and van der Werf, G. R.: Analysis of daily, monthly, and
663 annual burned area using the fourth-generation global fire emissions database
664 (GFED4), *J. Geophys. Res. Biogeosciences*, 118, 317–328, doi:10.1002/jgrg.20042,
665 2013, 2013.
- 666 Gilbert, M., Nicolas, G., Cinardi, G., Van Boeckel, T. P., Vanwambeke, S. O., Wint,
667 G. R. W. and Robinson, T. P.: Global distribution data for cattle, buffaloes, horses,
668 sheep, goats, pigs, chickens and ducks in 2010, *Sci. Data*, 5, 1–11,
669 doi:10.1038/sdata.2018.227, 2018.
- 670 Hauglustaine, D. A., Hourdin, F., Jourdain, L., Filiberti, M.-A., Walters, S., Lamarque,
671 J.-F. and Holland, E. A.: Interactive chemistry in the Laboratoire de Meteorologie
672 Dynamique general circulation model: Description and background tropospheric
673 chemistry evaluation, *J. Geophys. Res.*, 109(D04314), doi:10.1029/2003JD003957,
674 2004.
- 675 Hauglustaine, D. A., Balkanski, Y. and Schulz, M.: A global model simulation of
676 present and future nitrate aerosols and their direct radiative forcing of climate, *Atmos.*
677 *Chem. Phys.*, 14(20), 11031–11063, doi:10.5194/acp-14-11031-2014, 2014.
- 678 Henze, D. K., Shindell, D. T., Akhtar, F., Spurr, R. J. D., Pinder, R. W., Loughlin, D.,
679 Kopacz, M., Singh, K. and Shim, C.: Spatially Refined Aerosol Direct Radiative
680 Forcing Efficiencies, *Environ. Sci. Technol.*, 46, 9511–9518, doi:10.1021/es301993s,
681 2012.
- 682 Hersbach, H., Bell, B., Berrisford, P., Hirahara, S., Horányi, A., Muñoz-Sabater, J.,
683 Nicolas, J., Peubey, C., Radu, R., Schepers, D., Simmons, A., Soci, C., Abdalla, S.,
684 Abellan, X., Balsamo, G., Bechtold, P., Biavati, G., Bidlot, J., Bonavita, M., De
685 Chiara, G., Dahlgren, P., Dee, D., Diamantakis, M., Dragani, R., Flemming, J.,
686 Forbes, R., Fuentes, M., Geer, A., Haimberger, L., Healy, S., Hogan, R. J., Hólm, E.,
687 Janisková, M., Keeley, S., Laloyaux, P., Lopez, P., Lupu, C., Radnoti, G., de Rosnay,
688 P., Rozum, I., Vamborg, F., Villaume, S. and Thépaut, J. N.: The ERA5 global



- 689 reanalysis, Q. J. R. Meteorol. Soc., 146(730), 1999–2049, doi:10.1002/qj.3803, 2020.
- 690 Hourdin, F. and Armengaud, A.: The Use of Finite-Volume Methods for Atmospheric
- 691 Advection of Trace Species. Part I: Test of Various Formulations in a General
- 692 Circulation Model, Mon. Weather Rev., 127(5), 822–837, doi:10.1175/1520-
- 693 0493(1999)127<0822:TUOFVM>2.0.CO;2, 1999.
- 694 Hourdin, F., Musat, I., Bony, S., Braconnot, P., Codron, F., Dufresne, J. L., Fairhead,
- 695 L., Filiberti, M. A., Friedlingstein, P., Grandpeix, J. Y., Krinner, G., LeVan, P., Li, Z. X.
- 696 and Lott, F.: The LMDZ4 general circulation model: Climate performance and
- 697 sensitivity to parametrized physics with emphasis on tropical convection, Clim. Dyn.,
- 698 27(7–8), 787–813, doi:10.1007/s00382-006-0158-0, 2006.
- 699 Kharol, S. K., Shephard, M. W., McLinden, C. A., Zhang, L., Sioris, C. E., O'Brien, J.
- 700 M., Vet, R., Cady-Pereira, K. E., Hare, E., Siemons, J. and Krotkov, N. A.: Dry
- 701 Deposition of Reactive Nitrogen From Satellite Observations of Ammonia and
- 702 Nitrogen Dioxide Over North America, Geophys. Res. Lett., 45(2), 1157–1166,
- 703 doi:10.1002/2017GL075832, 2018.
- 704 Klimont, Z.: personal communication, 2022.
- 705 Klimont, Z., Kupiainen, K., Heyes, C., Purohit, P., Cofala, J., Rafaj, P., Borken-
- 706 Kleefeld, J. and Schöpp, W.: Global anthropogenic emissions of particulate matter
- 707 including black carbon, Atmos. Chem. Phys., 17, 8681–8723, doi:10.5194/acp-17- 50
- 708 8681-2017, 2017.
- 709 Krupa, S. V.: Effects of atmospheric ammonia (NH₃) on terrestrial vegetation: A
- 710 review, Environ. Pollut., 124(2), 179–221, doi:10.1016/S0269-7491(02)00434-7,
- 711 2003.
- 712 Kuhn, T.: The revision of the German Fertiliser Ordinance in 2017, Agric. Resour.
- 713 Econ., 2(Discussion Paper), 1–22, 2017.
- 714 Lassaletta, L., Romero, E., Billen, G., Garnier, J., García-Gómez, H. and Rovira, J.
- 715 V.: Spatialized N budgets in a large agricultural Mediterranean watershed: High
- 716 loading and low transfer, Biogeosciences, 9(1), 57–70, doi:10.5194/bg-9-57-2012,
- 717 2012.
- 718 Lecina, S., Isidoro, D., Playán, E. and Aragüés, R.: Irrigation modernization in Spain:
- 719 Effects on water quantity and quality-a conceptual approach, Int. J. Water Resour.
- 720 Dev., 26(2), 265–282, doi:10.1080/07900621003655734, 2010.
- 721 Lelieveld, J., Evans, J. S., Fnais, M., Giannadaki, D. and Pozzer, A.: The contribution
- 722 of outdoor air pollution sources to premature mortality on a global scale., Nature,
- 723 525(7569), 367–71, doi:10.1038/nature15371, 2015.
- 724 Lesschen, J. P., van den Berg, M., Westhoek, H. J., Witzke, H. P. and Oenema, O.:
725 Greenhouse gas emission profiles of European livestock sectors, Anim. Feed Sci.
- 726 Technol., 166–167, 16–28, doi:10.1016/j.anifeedsci.2011.04.058, 2011.
- 727 Li, C., Martin, R. V., Shephard, M. W., Pereira, K. C., Cooper, M. J., Kaiser, J., Lee,
- 728 C. J., Zhang, L. and Henze, D. K.: Assessing the Iterative Finite Difference Mass
- 729 Balance and 4D - Var Methods to Derive Ammonia Emissions Over North America
- 730 Using Synthetic Observations, J. Geophys. Res. Atmos., 124, 4222–4236,
- 731 doi:10.1029/2018JD030183, 2019.
- 732 Lonati, G. and Cernuschi, S.: Temporal and spatial variability of atmospheric
- 733 ammonia in the Lombardy region (Northern Italy), Atmos. Pollut. Res., 11(12), 2154–
- 734 2163, doi:10.1016/j.apr.2020.06.004, 2020.
- 735 Luo, Z., Zhang, Y., Chen, W., Van Damme, M., Coheur, P.-F. and Clarisse, L.:
736 Estimating global ammonia (NH₃) emissions based on IASI observations from 2008
- 737 to 2018, Atmos. Chem. Phys., 22(15), 10375–10388, doi:10.5194/acp-22-10375-
- 738 2022, 2022.



- 739 Malm, W. C.: Spatial and monthly trends in speciated fine particle concentration in
740 the United States, *J. Geophys. Res.*, 109(D3), D03306, doi:10.1029/2003JD003739,
741 2004.
- 742 McDuffie, E., Smith, S., O'Rourke, P., Tibrewal, K., Venkataraman, C., Marais, E.,
743 Zheng, B., Crippa, M., Brauer, M. and Martin, R.: A global anthropogenic emission
744 inventory of atmospheric pollutants from sector- and fuel-specific sources (1970–
745 2017): An application of the Community Emissions Data System (CEDS), *Earth Syst.*
746 *Sci. Data Discuss.*, 1–49, doi:10.5194/essd-2020-103, 2020.
- 747 Montalvo, G., Pineiro, C., Herrero, M., Biegeriego, M. and Prins, W.: Ammonia
748 Abatement by Animal Housing Techniques BT - Costs of Ammonia Abatement and
749 the Climate Co-Benefits, edited by S. Reis, C. Howard, and M. A. Sutton, pp. 53–73,
750 Springer Netherlands, Dordrecht., 2015.
- 751 Paulot, F., Jacob, D. J., Pinder, R. W., Bash, J. O., Travis, K. and Henze, D. K.:
752 Ammonia emissions in the United States, European Union, and China derived by
753 high-resolution inversion of ammonium wet deposition data: Interpretation with a new
754 agricultural emissions inventory (MASAGE-NH₃), *J. Geophys. Res. Atmos.*, 119(7),
755 4343–4364, doi:10.1002/2013JD021130, 2014.
- 756 Pisso, I., Sollum, E., Grythe, H., Kristiansen, N., Cassiani, M., Eckhardt, S., Arnold,
757 D., Morton, D., Thompson, R. L., Groot Zwaaftink, C. D., Evangeliou, N., Sodemann,
758 H., Haimberger, L., Henne, S., Brunner, D., Burkhardt, J. F., Fouilloux, A., Brioude, J.,
759 Philipp, A., Seibert, P. and Stohl, A.: The Lagrangian particle dispersion model
760 FLEXPART version 10.4, *Geosci. Model Dev.*, 12, 4955–4997, doi:10.5194/gmd-12-
761 4955-2019, 2019.
- 762 Pope, C. A. and Dockery, D. W.: Health effects of fine particulate air pollution: Lines
763 that connect, *J. Air Waste Manag. Assoc.*, 56(6), 709–742,
764 doi:10.1080/10473289.2006.10464485, 2006.
- 765 Pope III, C. A., Burnett, R. T., Thun, M. J., Calle, E. E., Krewski, D. and Thurston, G.
766 D.: Lung Cancer, Cardiopulmonary Mortality, and Long-term Exposure to Fine
767 Particulate Air Pollution, *J. Am. Med. Assoc.*, 287(9), 1132–1141,
768 doi:10.1001/jama.287.9.1132, 2002.
- 769 Poteko, J., Zähler, M. and Schrade, S.: Effects of housing system, floor type and
770 temperature on ammonia and methane emissions from dairy farming: A meta-
771 analysis, *Biosyst. Eng.*, 182, 16–28, doi:10.1016/j.biosystemseng.2019.03.012, 2019.
- 772 Rodgers, C. D.: Inverse methods for atmospheres: Theory and practice., 2000.
- 773 Seinfeld, J. H. and Pandis, S. N.: Atmospheric Chemistry and Physics. From Air
774 Pollution to Climate Change, 2nd ed., John Wiley & Sons, NY., 2000.
- 775 Shephard, M. W. and Cady-Pereira, K. E.: Cross-track Infrared Sounder (CrIS)
776 satellite observations of tropospheric ammonia, *Atmos. Meas. Tech.*, 8(3), 1323–
777 1336, doi:10.5194/amt-8-1323-2015, 2015.
- 778 Shephard, M. W., McLinden, C. A., Cady-Pereira, K. E., Luo, M., Moussa, S. G.,
779 Leithead, A., Liggio, J., Staebler, R. M., Akingunola, A., Makar, P., Lehr, P., Zhang,
780 J., Henze, D. K., Millet, D. B., Bash, J. O., Zhu, L., Wells, K. C., Capps, S. L.,
781 Chaliyakunnel, S., Gordon, M., Hayden, K., Brook, J. R., Wolde, M. and Li, S. M.:
782 Tropospheric Emission Spectrometer (TES) satellite observations of ammonia,
783 methanol, formic acid, and carbon monoxide over the Canadian oil sands: Validation
784 and model evaluation, *Atmos. Meas. Tech.*, 8(12), 5189–5211, doi:10.5194/amt-8-
785 5189-2015, 2015.
- 786 Shephard, M. W., Damers, E., Cady-Pereira, K., Kharol, S., Thompson, J.,
787 Gainariu-Matz, Y., Zhang, J., A. McLinden, C., Kovachik, A., Moran, M., Bittman, S.,
788 E. Sioris, C., Griffin, D., J. Alvarado, M., Lonsdale, C., Savic-Jovicic, V. and Zheng,



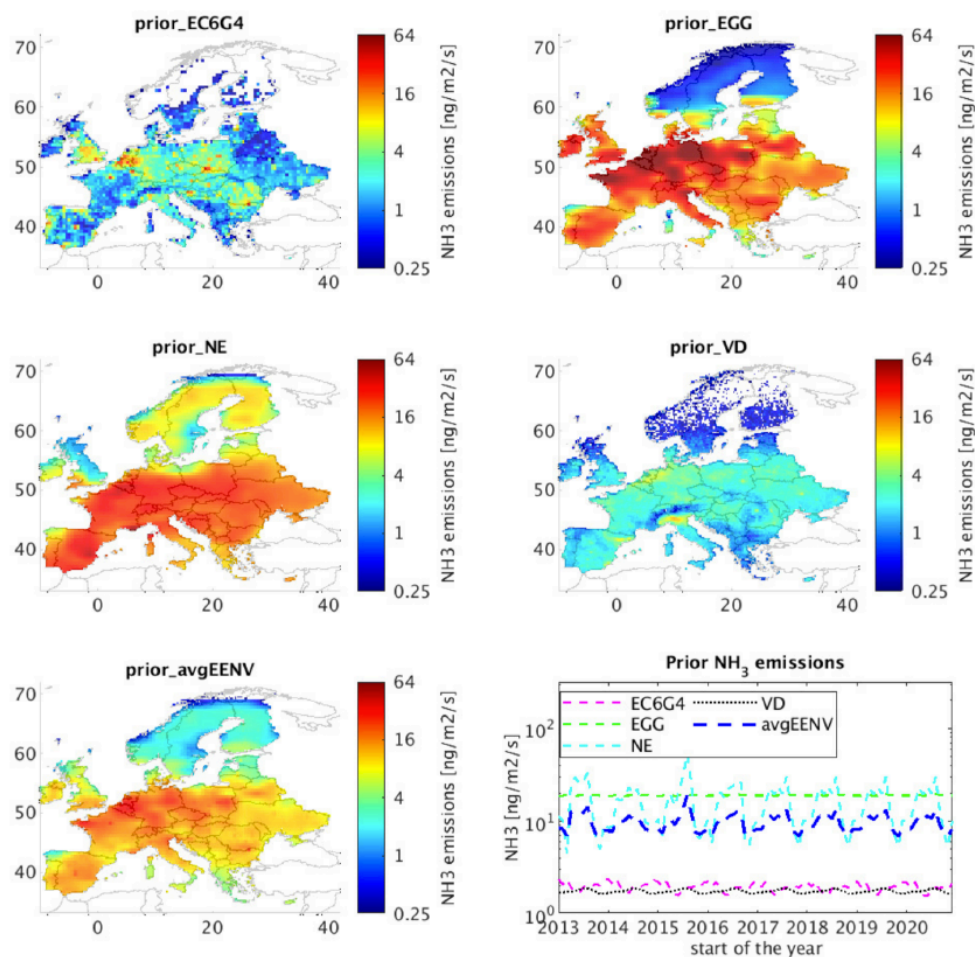
789 Q.: Ammonia measurements from space with the Cross-track Infrared Sounder:
790 Characteristics and applications, *Atmos. Chem. Phys.*, 20(4), 2277–2302,
791 doi:10.5194/acp-20-2277-2020, 2020.
792 Sigurdarson, J. J., Svane, S. and Karring, H.: The molecular processes of urea
793 hydrolysis in relation to ammonia emissions from agriculture, *Rev. Environ. Sci.*
794 *Biotechnol.*, 17(2), 241–258, doi:10.1007/s11157-018-9466-1, 2018.
795 Sitwell, M., Shephard, M. W., Rochon, Y., Cady-Pereira, K. and Dammers, E.: An
796 ensemble-variational inversion system for the estimation of ammonia emissions
797 using CrIS satellite ammonia retrievals, *Atmos. Chem. Phys.*, 22(10), 6595–6624,
798 doi:10.5194/acp-22-6595-2022, 2022.
799 Someya, Y., Imasu, R., Shiomi, K. and Saitoh, N.: Atmospheric ammonia retrieval
800 from the TANSO-FTS / GOSAT thermal infrared sounder, *Atmos. Meas. Tech.*, 13,
801 309–321, 2020.
802 Stevens, C. J., Dupr, C., Dorland, E., Gaudnik, C., Gowing, D. J. G., Bleeker, A.,
803 Diekmann, M., Alard, D., Bobbink, R., Fowler, D., Corcket, E., Mountford, J. O.,
804 Vandvik, V., Aarrestad, P. A., Muller, S. and Dise, N. B.: Nitrogen deposition
805 threatens species richness of grasslands across Europe, *Environ. Pollut.*, 158(9),
806 2940–2945, doi:10.1016/j.envpol.2010.06.006, 2010.
807 Stohl, A., Forster, C., Frank, A., Seibert, P. and Wotawa, G.: Technical note: The
808 Lagrangian particle dispersion model FLEXPART version 6.2, *Atmos. Chem. Phys.*,
809 5(9), 2461–2474, doi:10.5194/acp-5-2461-2005, 2005.
810 Sutton, M. A., Erisman, J. W., Dentener, F. and Möller, D.: Ammonia in the
811 environment: From ancient times to the present, *Environ. Pollut.*, 156(3), 583–604,
812 doi:10.1016/j.envpol.2008.03.013, 2008.
813 Sutton, M. A., Reis, S., Riddick, S. N., Dragosits, U., Nemitz, E., Theobald, M. R.,
814 Tang, Y. S., Braban, C. F., Vieno, M., Dore, A. J., Mitchell, R. F., Wanless, S., Daunt,
815 F., Fowler, D., Blackall, T. D., Milford, C., Flechard, C. R., Loubet, B., Massad, R.,
816 Cellier, P., Personne, E., Coheur, P. F., Clarisse, L., Damme, M. Van, Ngadi, Y.,
817 Clerbaux, C., Skjøth, C. A., Geels, C., Hertel, O., Kruit, R. J. W., Pinder, R. W., Bash,
818 J. O., Walker, J. T., Simpson, D., Horvath, L., Misselbrook, T. H., Bleeker, A.,
819 Dentener, F. and Vries, W. de: Towards a climate-dependent paradigm of ammonia
820 emission and deposition, *Philos. Trans. R. Soc. B Biol. Sci.*, 368(1621), 20130166–
821 20130166, doi:10.1098/rstb.2013.0166, 2013.
822 Tang, Y. S., Flechard, C., Dämmgen, U., Vidic, S., Djuricic, V., Mitosinkova, M.,
823 Uggerud, H., Sanz, M., Simmons, I., Dragosits, U., Nemitz, E., Twigg, M., van Dijk,
824 N., Fauvel, Y., Sanz-Sanchez, F., Ferm, M., Perrino, C., Catrambone, M., Leaver, D.,
825 Braban, C., Cape, J. N., Heal, M. and Sutton, M.: Pan-European rural atmospheric
826 monitoring network shows dominance of NH_3 gas and
827 NH_4 and NO_3 aerosol in inorganic pollution
828 load, *Atmos. Chem. Phys. Discuss.*, 1–61, 2020.
829 Tichý, O., Šmídl, V., Hofman, R. and Stohl, A.: LS-APC v1.0: A tuning-free method
830 for the linear inverse problem and its application to source-Term determination,
831 *Geosci. Model Dev.*, 9(11), 4297–4311, doi:10.5194/gmd-9-4297-2016, 2016.
832 Tichý, O., Ulrych, L., Šmídl, V., Evangeliou, N. and Stohl, A.: On the tuning of
833 atmospheric inverse methods: Comparisons with the European Tracer Experiment
834 (ETEX) and Chernobyl datasets using the atmospheric transport model FLEXPART,
835 *Geosci. Model Dev.*, 13(12), 5917–5934, doi:10.5194/gmd-13-5917-2020, 2020.
836 Tichý, O., Otervik, M. S., Eckhardt, S., Balkanski, Y., Hauglustaine, D. and
837 Evangeliou, N.: NH_3 emissions over Europe during COVID-19 were modulated by
838 changes in atmospheric chemistry, *Commun. Earth Environ.*, in review, 1–13,



839 doi:10.21203/rs.3.rs-1930069/v1, 2022.
840 Torseth, K., Aas, W., Breivik, K., Fjeraa, A. M., Fiebig, M., Hjellbrekke, A. G., Lund
841 Myhre, C., Solberg, S. and Yttri, K. E.: Introduction to the European Monitoring and
842 Evaluation Programme (EMEP) and observed atmospheric composition change
843 during 1972-2009, *Atmos. Chem. Phys.*, 12(12), 5447–5481, doi:10.5194/acp-12-
844 5447-2012, 2012.
845 Tsimpidi, A. P., Karydis, V. A. and Pandis, S. N.: Response of inorganic fine
846 particulate matter to emission changes of sulfur dioxide and ammonia: The Eastern
847 United States as a case study, *J. Air Waste Manag. Assoc.*, 57(12), 1489–1498,
848 doi:10.3155/1047-3289.57.12.1489, 2007.
849 Velthof, G. L., van Bruggen, C., Groenestein, C. M., de Haan, B. J., Hoogeveen, M.
850 W. and Huijsmans, J. F. M.: A model for inventory of ammonia emissions from
851 agriculture in the Netherlands, *Atmos. Environ.*, 46, 248–255,
852 doi:10.1016/j.atmosenv.2011.09.075, 2012.
853 Vira, J., Hess, P., Melkonian, J. and Wieder, W. R.: An improved mechanistic model
854 for ammonia volatilization in Earth system models: Flow of Agricultural Nitrogen
855 version 2 (FANv2), *Geosci. Model Dev.*, 13(9), 4459–4490, doi:10.5194/gmd-13-
856 4459-2020, 2020.
857 van Vuuren, A. M., Pineiro, C., van der Hoek, K. W. and Oenema, O.: Economics of
858 Low Nitrogen Feeding Strategies BT - Costs of Ammonia Abatement and the
859 Climate Co-Benefits, edited by S. Reis, C. Howard, and M. A. Sutton, pp. 35–51,
860 Springer Netherlands, Dordrecht., 2015.
861 Warner, J. X., Dickerson, R. R., Wei, Z., Strow, L. L., Wang, Y. and Liang, Q.:
862 Increased atmospheric ammonia over the world's major agricultural areas detected
863 from space, *Geophys. Res. Lett.*, 44, 1–10, doi:10.1002/2016GL072305, 2017.
864 Whitburn, S., Van Damme, M., Clarisse, L., Bauduin, S., Heald, C. L., Hadji-Lazaro,
865 J., Hurtmans, D., Zondlo, M. A., Clerbaux, C. and Coheur, P. F.: A flexible and robust
866 neural network IASI-NH₃ retrieval algorithm, *J. Geophys. Res.*, 121(11), 6581–6599,
867 doi:10.1002/2016JD024828, 2016.
868 Zavyalov, V., Esplin, M., Scott, D., Esplin, B., Bingham, G., Hoffman, E., Lietzke, C.,
869 Predina, J., Frain, R., Suwinski, L., Han, Y., Major, C., Graham, B. and Phillips, L.:
870 Noise performance of the CrIS instrument, , 118, 108–120,
871 doi:10.1002/2013JD020457, 2013.
872 Zhu, L., Henze, D. K., Cady-Pereira, K. E., Shephard, M. W., Luo, M., Pinder, R. W.,
873 Bash, J. O. and Jeong, G. R.: Constraining U.S. ammonia emissions using TES
874 remote sensing observations and the GEOS-Chem adjoint model, *J. Geophys. Res.*
875 *Atmos.*, 118(8), 3355–3368, doi:10.1002/jgrd.50166, 2013.
876
877



878 **FIGURES & LEGENDS**



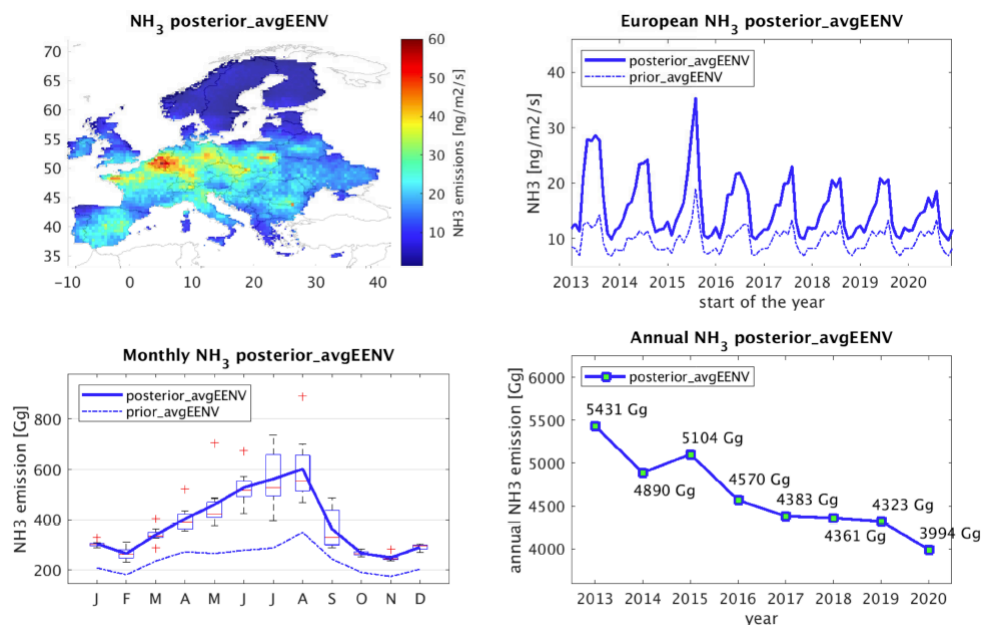
879

880 **Figure 1.** Four ammonia prior emissions (EC6G4, EGG, NE, VD) are displayed in the first two

881 rows. The combined prior (avgEENV) is displayed in the bottom left. The temporal activity of

882 all five prior emissions is given in bottom right.

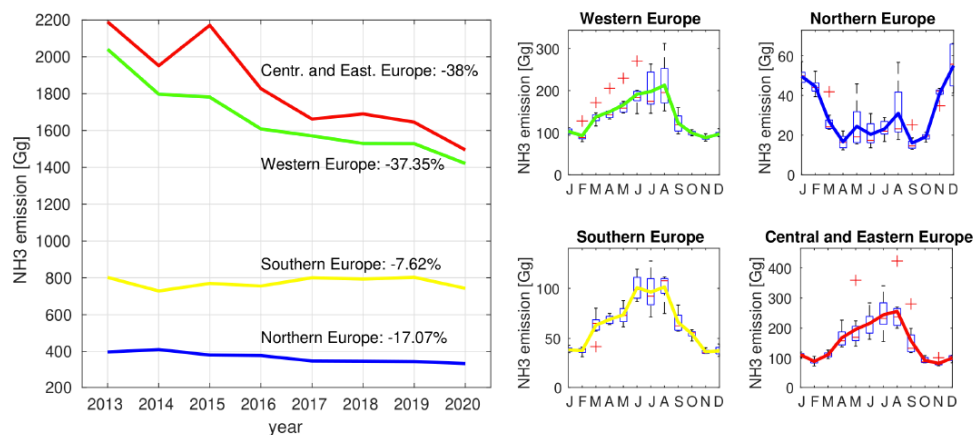
883



884

885 **Figure 2.** The spatial distribution of posterior ammonia emissions (posterior_EENV, top-left)
 886 together with its temporal distribution (top-right). Monthly average (bottom-left) and annually
 887 average (bottom-right) estimates are also plotted. The monthly average posterior emissions are
 888 accompanied by the box plot where the red line indicates the median, the bottom and top edges
 889 of the Boxes indicating the 25th and 75th percentiles, respectively, and the whiskers extend to
 890 the most extreme data points not considered as outliers, which are denoted using red crosses.
 891 Solid blue lines refer to the posterior ammonia emissions, while dashed ones to the prior
 892 emissions (avgEENV).

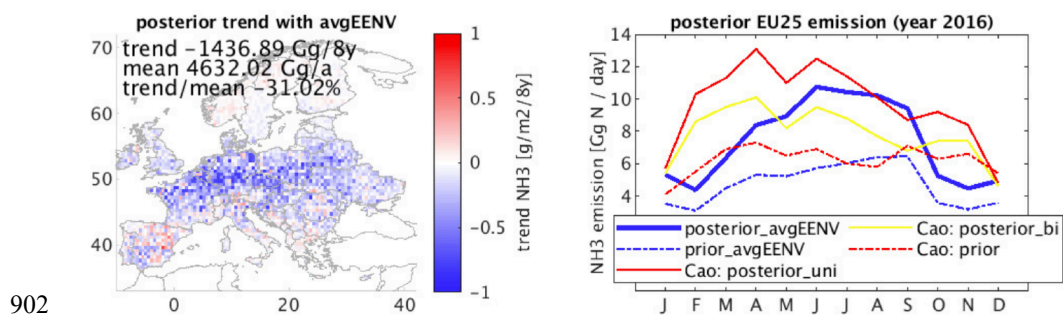
893



894

895 **Figure 3.** Left: Annual posterior emissions of ammonia in Southern (yellow), Western (green),
 896 Northern (blue), and Central and Eastern (red) Europe. Right: Monthly average posterior
 897 emissions of ammonia accompanied by box plots, where the red line indicates the median, the
 898 bottom and top edges of the box indicate the 25th and 75th percentiles, respectively, and the
 899 whiskers extend to the most extreme data points (not considered outliers), which are represented
 900 using red crosses.

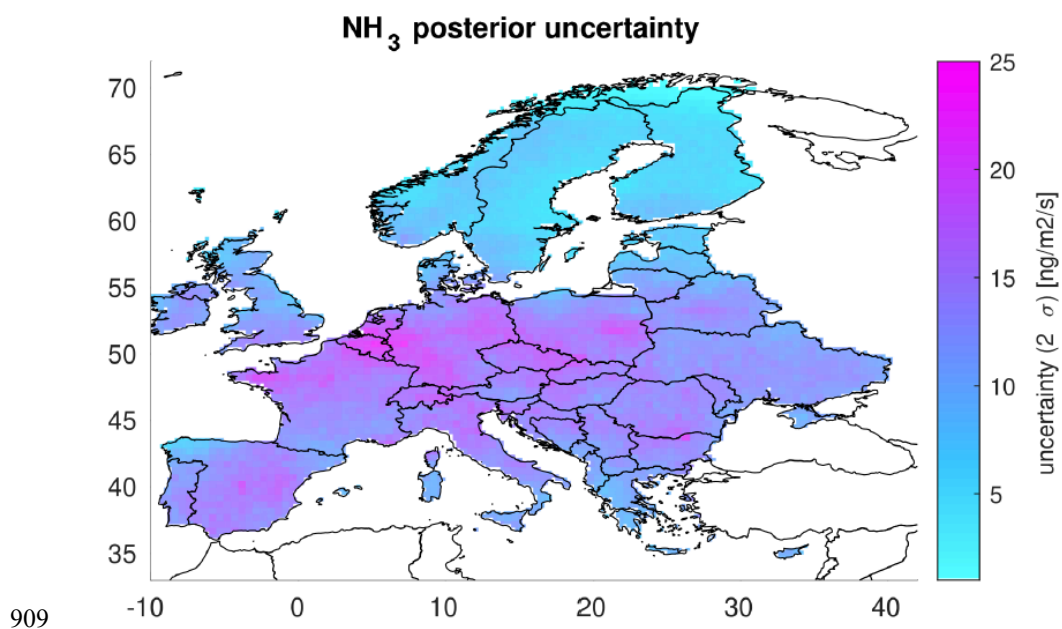
901



902

903 **Figure 4.** Left: spatial distribution of ammonia emission trends computed for the studied period
904 2013–2020 in the same way as in (Luo et al., 2022), where also trend, mean, and trend/mean
905 are defined/computed in the same way. Right: comparison of ammonia emissions from the
906 EU25 countries for the year 2016 from our posterior calculations (posterior_avgEENV, blue)
907 and results from Cao et al. (2022) (posterior_uni in red and posterior_bi, in yellow).

908



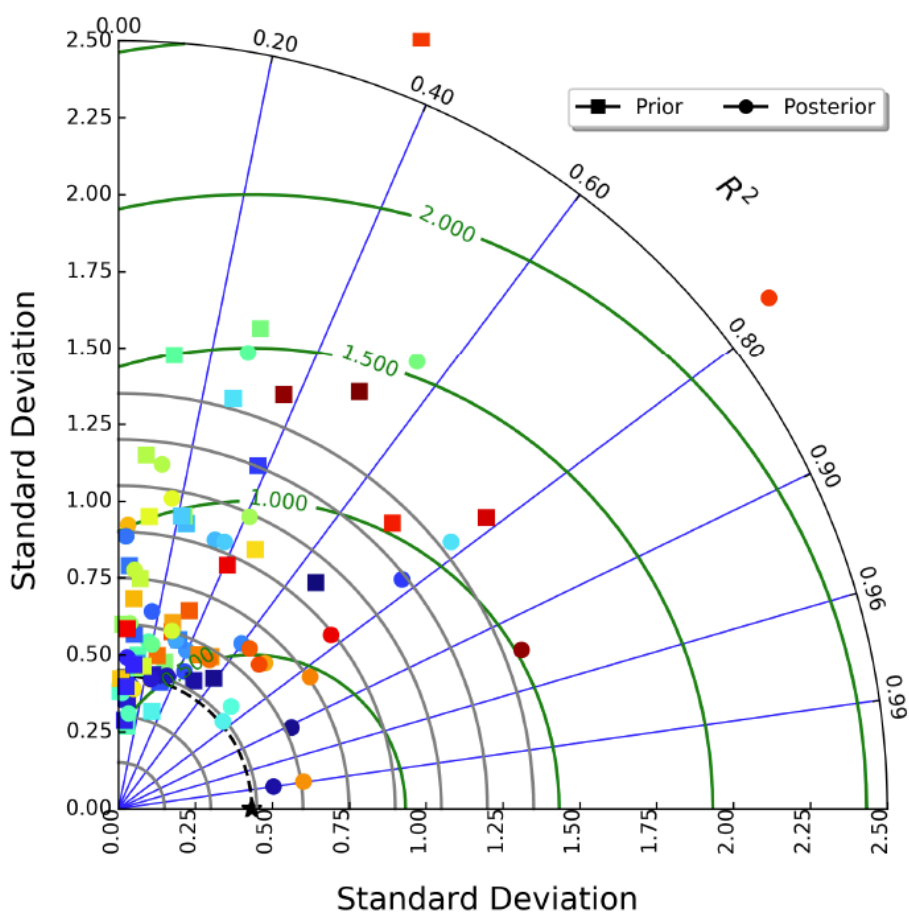
910 **Figure 5.** Absolute uncertainty of posterior emissions of ammonia calculated as 2σ averaged
911 for the whole study period 2013–2020.

912



Comparison with EMEP observations

★Ref.	DK0003	ES0009	GB0013	NL0091	SE0011	DE0009	GB1055
AM0001	DK0008	FI0009	GB0014	NO0002	SE0012	ES0014	HU0003
BE0014	DK0012	FI0017	GB0048	NO0015	SE0014	LV0010	SE0020
CH0002	DK0031	FI0022	GB0054	NO0039	SK0006	NL0007	CH0053
CH0005	ES0001	FI0036	GE0001	NO0056	DE0001	SI0008	FI0050
DE0002	ES0007	FI0037	HU0002	PL0005	DE0003	FI0018	SE0022
DE0007	ES0008	GB0006	IT0001	SE0005	DE0008		



913

914 **Figure 6.** Modelled concentrations of ammonia with prior and posterior emissions against
 915 ground-based observations from 53 EMEP stations for 2013–2020 presented in a Taylor
 916 diagram. The diagram shows the Pearson’s correlation coefficient (gauging similarity in pattern
 917 between the modelled and observed concentrations) that is related to the azimuthal angle (blue
 918 contours); the standard deviation of modelled concentrations of ammonia is proportional to the
 919 radial distance from the origin (black contours) and the centered normalized RMSE of modelled
 920 concentrations is proportional to the distance from the reference standard deviation (green
 921 contours).

922